

Enhanced anisotropic superconductivity in the topological nodal-line semimetal In_xTaS_2

Yupeng Li,^{1,2,*} Zhongxiu Wu,¹ Jingang Zhou,¹ Kunliang Bu,¹ Chenchao Xu,¹ Lei Qiao,¹ Miaocong Li,¹ Hua Bai,¹ Jiang Ma,¹ Qian Tao,¹ Chao Cao,³ Yi Yin,^{1,4} and Zhu-An Xu^{1,2,4,†}

¹*Zhejiang Province Key Laboratory of Quantum Technology and Device,
Department of Physics, Zhejiang University, Hangzhou 310027, China*

²*State Key Laboratory of Silicon Materials, Zhejiang University, Hangzhou 310027, China*

³*Department of Physics, Hangzhou Normal University, Hangzhou 310036, China*

⁴*Collaborative Innovation Centre of Advanced Microstructures, Nanjing University, Nanjing 210093, China*

(Dated: November 16, 2020)

Coexistence of topological bands and charge density wave (CDW) in topological materials has attracted immense attentions because of their fantastic properties, such as axionic-CDW, three-dimensional quantum Hall effect, etc. In this work, a nodal-line semimetal In_xTaS_2 characterized by CDW and superconductivity is successfully synthesized, whose structure and topological bands (two separated Weyl rings) are similar to $\text{In}_{0.58}\text{TaSe}_2$. A 2×2 commensurate CDW is observed at low temperature in In_xTaS_2 , identified by transport properties and STM measurements. Moreover, superconductivity emerges below 0.69 K, and the anisotropy ratio of upper critical field [$\Gamma = H_{c2}^{\parallel ab}(0)/H_{c2}^{\parallel c}(0)$] is significantly enhanced compared to 2H-TaS_2 , which shares the same essential layer unit. According to the Lawrence-Doniach model, the enhanced Γ may be explained by the reduced effective mass in $k_x - k_y$ plane, where Weyl rings locate. Therefore, this type of layered topological systems may offer a platform to investigate highly anisotropic superconductivity and to understand the extremely large upper critical field in the bulk or in the two-dimensional limit.

I. INTRODUCTION

Topological nodal-line semimetals (TNLSMs)¹ have been attracting tremendous attentions due to the closed loop of band crossing formed in momentum space. Typical TNLSMs have been experimentally reported in the so-called 112 systems (In_xTaSe_2 ² and PbTaSe_2 ³), LiFeAs structure (ZrSiS ⁴), PtSn_4 ⁵ and so on. Unlike the zero-dimensional nodal points in Dirac semimetals⁶⁻⁸ and Weyl semimetals⁹⁻¹⁴, the one-dimensional (1D) nodal lines can be protected by certain symmetry¹⁵ no matter whether the spin-orbital coupling (SOC) is included. Several intriguing properties have been predicted and experimentally observed in TNLSMs, such as drumhead surface states^{3,16,17}, anomalous quantum oscillations¹⁸, three-dimensional quantum Hall effect (3D QHE)¹⁹, and topological superconductivity²⁰. As regards searching for bulk topological superconductors (TSCs), one of the employed strategies is to induce superconductivity in topological materials²¹ through the application of high pressure²²⁻²⁴, intercalation between layers^{3,25}, or chemical doping^{3,25}, etc.

Among these approaches, intercalation of atoms and molecules into the layered transition-metal dichalcogenides (TMDs) MX_2 (M is the transition metal, $X = S, \text{Se}, \text{Te}$) and other layered compounds is an effective one to significantly modify their properties. For example, superconductivity can be induced in Cu_xTiSe_2 ²⁶ and $\text{Cu}_x\text{Bi}_2\text{Se}_3$ ²⁵; the intercalated graphite exhibits more ex-

cellent electric and optical features²⁷, which greatly contributes to extensive applications; the TNLSM PbTaSe_2 viewed as Pb atoms intercalation in TaSe_2 introduces not only topological bands, such as InTaSe_2 ², TlTaSe_2 ¹⁶, InNbS_2 , and InNbSe_2 ²⁸, but also possible Majorana bound states in the superconducting vortices^{20,29}. Moreover, the intercalated layered compounds possibly host the higher superconducting transition (T_c) or highly anisotropic superconductivity^{30,31}.

In this paper, the In-intercalated TNLSM In_xTaS_2 hosting both superconductivity and charge density wave (CDW) is successfully synthesized. It has the same structure and similar topological bands as InTaSe_2 ², whose two separate Weyl rings exist at the H point. It is a little different that the only one 2×2 commensurate CDW (CCDW) remains. The superconductivity is observed, and the extremely large anisotropy ratio of upper critical field is obtained in four samples, which may be related to the small effective mass in the ab plane.

II. EXPERIMENT

The polycrystalline InTaS_2 and single crystals In_xTaS_2 were prepared using the solid-state reaction method and the vapor transport method, respectively, also referred to In_xTaSe_2 ². The x-ray diffraction (XRD) data were collected using a monochromatic $\text{Cu K}\alpha_1$ radiation. An energy-dispersive x-ray spectroscopy (EDS) was employed to analyze chemical compositions of samples. A standard six-probe technique was carried out to measure the longitudinal resistivity and Hall resistivity on an Oxford ³He-based cryostat and a physical properties measurement system (PPMS). Scanning tunneling mi-

* yupengLi@zju.edu.cn

† zhuan@zju.edu.cn

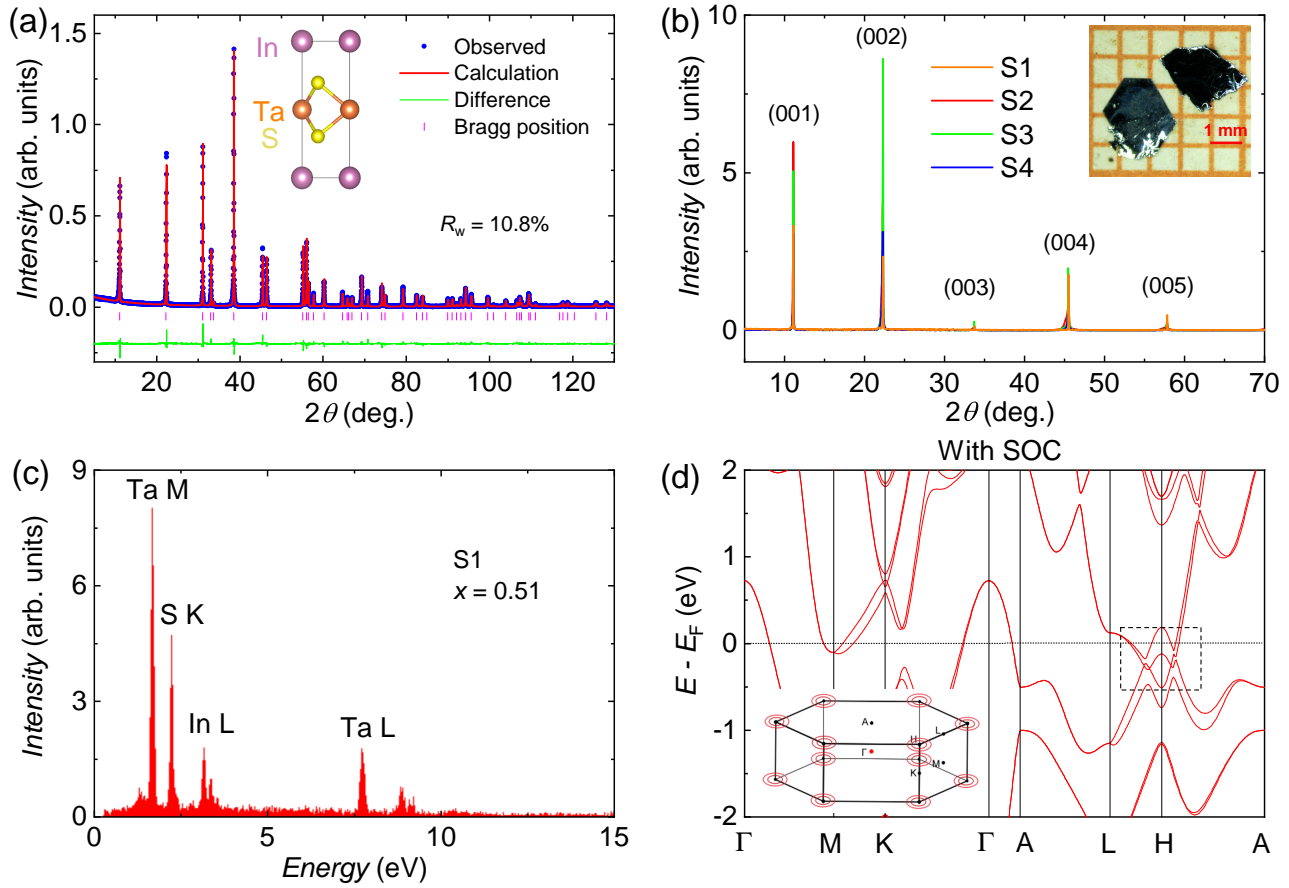


FIG. 1. (a) Rietveld refinement of powder XRD data for polycrystalline InTaS_2 . The inset is a side view of the InTaS_2 structure. (b) XRD spectrum for the $(00l)$ facet of single crystals In_xTaS_2 . The optical photograph of two selected samples are shown in the inset. (c) One of typical EDS spectrums collected on these flat clean surfaces of single crystals. The In content x is between 0.51 and 0.59. (d) Band structures of InTaS_2 with SOC. Two separated Weyl rings appear at the H point in the first Brillouin zone, as shown in the inset.

croscopy (STM) measurements were performed in a commercial unisoku-UHV1500S STM system. The samples were cleaved in situ at ~ 77 K, then inserted into the STM measurement stage.

The density function theory (DFT) calculations were performed using the generalized gradient approximation (GGA) method and the Perdew-Burke-Ernzerhoff (PBE) exchange correlation functional. The lattice constants and the atomic coordinates were used from Rietveld-refined XRD data. A $18 \times 18 \times 6$ Monkhorst-Pack k -point mesh and SOC were applied in the computations.

III. RESULTS

A. Structure and topological bands

InTaS_2 has the same noncentrosymmetric structure $\bar{P}6m2$ as InTaSe_2 , as shown in the inset of Fig. 1(a),

the side view of the crystal structure. This structure can be well verified by the Rietveld refinement of polycrystalline powder XRD data [Fig. 1(a)]. The both reliable factor $R_{wp} = 10.8\%$ and small difference between observed data and calculations illustrate the good refinement. The refined lattice constants are $a = b = 3.3290$ Å and $c = 7.9891$ Å. High-quality single crystals In_xTaS_2 with various In content can be grown by the vapor transport method, and the plate-like samples are obtained as large as $3 \text{ mm} \times 2 \text{ mm}$ [inset of Fig. 1(b)]. Their XRD spectrums for the $(00l)$ facet are collected in Fig. 1(b), suggesting the good single crystal quality. The grown single crystals usually have a large amount of In vacancy. A typical EDS pattern of a In_xTaS_2 single-crystalline sample S1 is shown in Fig. 1(c), in which the chemical composition is $\text{In}:\text{Ta}:\text{S} = 0.51:1:2$. The x value of four In_xTaS_2 samples varies between 0.51 and 0.59, and phase separation easily emerges beyond this x range.

Fig. 1(d) shows the band structure of InTaS_2 with the

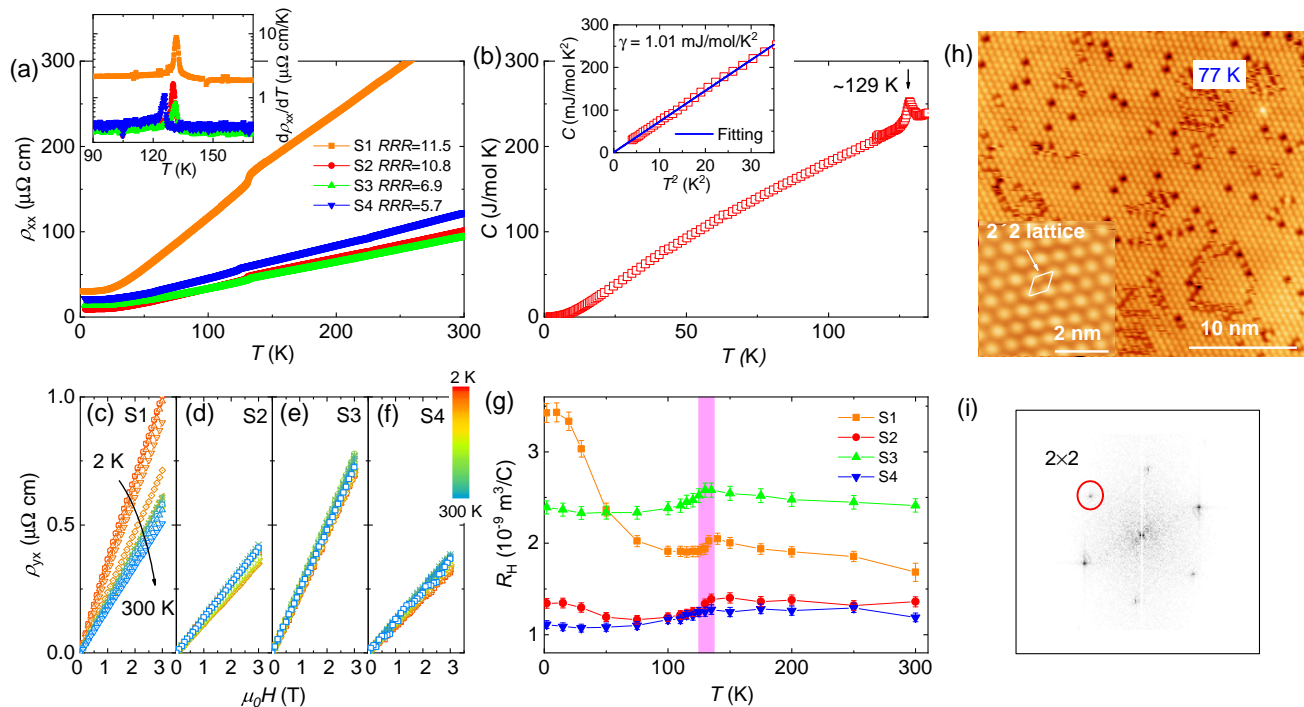


FIG. 2. (a) Electrical resistivity ρ_{xx} of four In_xTaS_2 samples exhibiting a CDW-like transition. The differential resistivity in the inset displays the transition temperatures ~ 130 K. (b) Low-temperature specific heat of In_xTaS_2 showing a distinct jump at ~ 129 K and zero magnetic field. The small $\gamma = 1.01 \text{ mJ mol}^{-1}\text{K}^{-2}$ is obtained in the inset. (c-f) Magnetic-field dependent ρ_{yx} at different temperatures. (g) Hall coefficients of four samples. The magenta range marks the transition. (h) STM images ($V_b = -1\text{V}$, $I_t = 20 \text{ pA}$) of the sample surface at 77 K. An enlarged range of a perfect surface is shown in the inset ($V_b = 1\text{V}$, $I_t = 100 \text{ pA}$), implying the 2×2 superlattice. (i) FFT image of (h). The 2×2 CCDW is marked by the red circle.

inclusion of SOC obtained by the DFT calculations. The main features are quite similar to the other 112 systems, such as InTaSe_2^2 , InNbS_2^{28} , PbTaSe_2^3 , and TlTaSe_2^{16} . The band inversion exists at the H point due to the hybridization of a hole pocket from Ta-5d orbitals and an electron pocket derived from In-5p orbitals. When the mirror reflection with respect to the In atomic plane is taken into consideration, these inversed bands are topological invariant. The four-fold-degenerate Dirac-type nodal ring splits into a pair of two-fold-degenerate nodal rings (Weyl rings) at the H point in the presence of SOC, as seen in the inset of Fig. 1(d). These Weyl rings remain gapless as a result of the symmetry protection, and they locate at $E - E_F \sim -0.25 \text{ eV}$, slightly below the Fermi level. Interestingly, the In vacancy in In_xTaS_2 is supposed to shift the Fermi level down to the Weyl rings, which is also observed in $\text{In}_{0.58}\text{TaSe}_2^2$. Each Weyl ring possesses a Berry phase of π , and they can be connected by drumhead surface states, a kind of nearly flat bands, which may exhibit a van Hove singularity, as discussed in Refs[3,16,28,32]^{3,16,17,28}.

B. CDW states

More fantastic features can be observed in the temperature dependence of resistivity for In_xTaS_2 , shown in Fig. 2. Fig. 2(a) shows the residual resistivity ratios (RRR) of samples S1, S2, S3, and S4 are 11.5, 10.8, 6.9, and 5.7, respectively. All resistivity curves exhibit one sudden drop at ~ 130 K, a little different from two CDW transitions in $\text{In}_{0.58}\text{TaSe}_2^2$. The transition temperatures can be identified by the differential resistivity in the inset of Fig. 2(a), and also confirmed by the jump of specific heat at ~ 129 K in Fig. 2(b). The small $\gamma = 1.01 \text{ mJ/mol/K}^2$ is obtained by fitting the low-temperature specific heat [inset of Fig. 2(b)]. In Fig. 2(c-f), the positive and linear Hall resistivity as a function of magnetic field (H) indicates the dominated carrier is hole in this system. In Fig. 2(g), the associated transitions of Hall coefficients (R_H) are also observed in the magenta range of temperature, in agreement with the longitudinal resistivity and specific heat measurements. Upon decreasing temperature, R_H decreases at this transition point in In_xTaS_2 , different from the increase of R_H in $\text{In}_{0.58}\text{TaSe}_2^2$. This behavior implies the possible distinct transition behavior or multiband feature, and the latter one is supposed to dominate here. The Hall

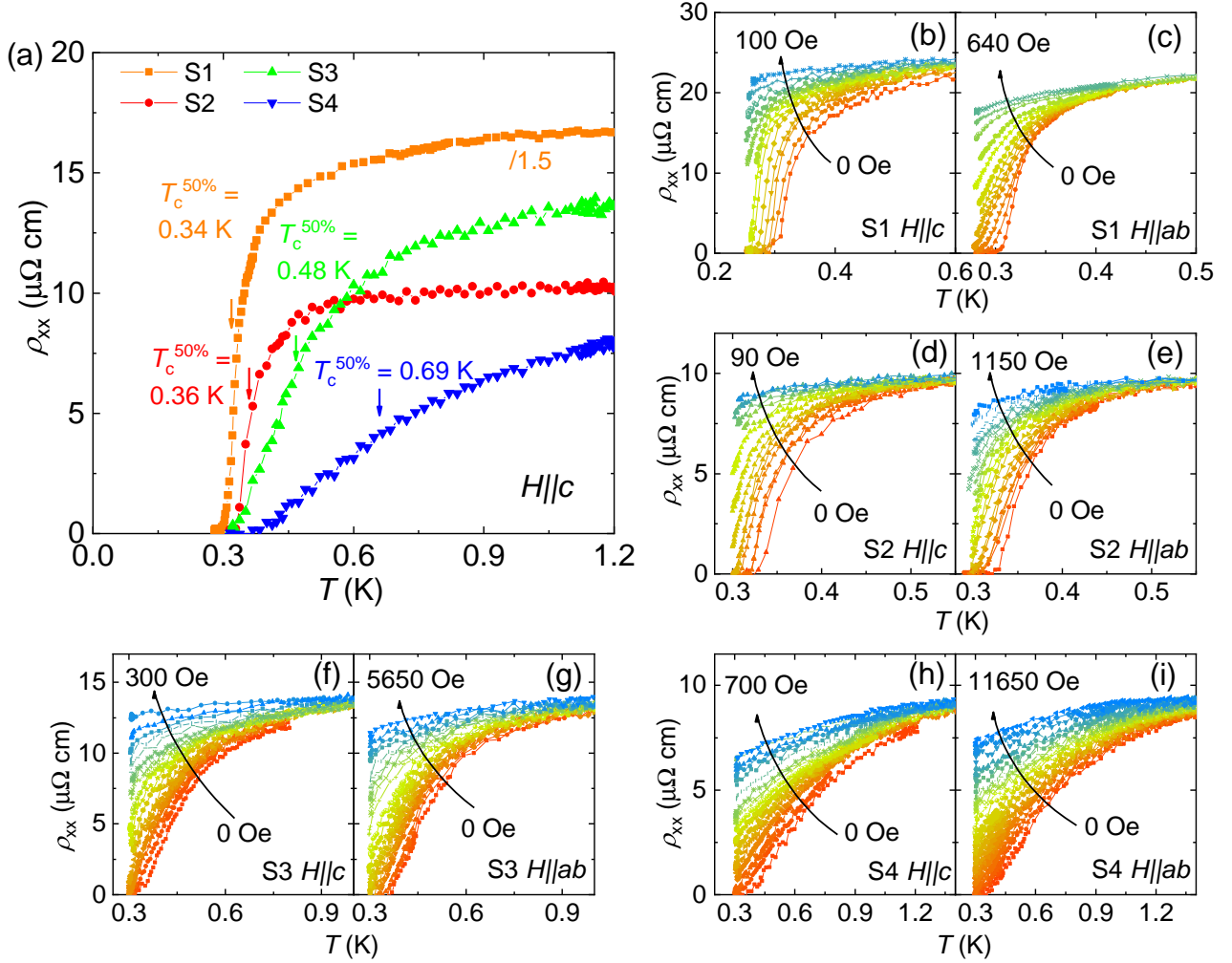


FIG. 3. (a) ρ_{xx} of samples S1, S2, S3, and S4 showing the superconducting transition at $T_c^{50\%} = 0.34$ K, 0.36 K, 0.48 K, and 0.69 K, respectively. $T_c^{50\%}$ is determined by 50% drop of the normal-state resistivity. (b-i) Temperature dependence of in-plane and out-of-plane resistivity for four samples.

coefficient in the multiband system, such as In_xTaS_2 , can be approximately described by the two-band model $R_H = [R_H^h(\sigma_{xx}^h)^2 - R_H^e(\sigma_{xx}^e)^2]/(\sigma_{xx}^h + \sigma_{xx}^e)^{232}$, where R_H^h and R_H^e denote the Hall coefficient for hole and electron, respectively, σ_{xx}^h and σ_{xx}^e are the hole conductivity and electron conductivity, respectively. Therefore, the Hall coefficient of the multiband system changes much complicatedly, especially in CDW systems, where band gaps emerge.

To further investigate this transition, we perform STM measurements at liquid nitrogen temperature (77 K). In Fig. 2(h), we show a STM topography obtained with a bias voltage $V_b = -1$ V and a tunneling current $I_t = 20$ pA, from which a triangular lattice can be observed. The triangular lattice can be further discerned in an enlarged small-area topography [inset of Fig. 2(f)]. The distance between adjacent bright spots is 6.951 Å (\sim

$2a$, a is the lattice constant). The basic element of lattice is the 2×2 superlattice, instead of the 1×1 atomic lattice. The superlattice is also confirmed in the fast Fourier-transformed (FFT) result in Fig. 2(i). The pattern marked by the red circle represents the 2×2 lattice, with a wave vector $\frac{1}{2}\vec{Q}_0$ ($\vec{Q}_0 = 4\pi/\sqrt{3}a$). The absence of atomic lattice in STM topography is similar to that for 1T-TaS₂^{33,34}. The low-temperature state below the transition is thus a 2×2 CCDW state. This type of 2×2 CCDW can also be observed in other intercalated MX_2 ³⁵, including $\text{In}_{0.58}\text{TaSe}_2$ ². In addition, the random black spots in Fig. 2(h) may stem from In atoms, which are randomly exfoliated from the In layer when the sample is cleaved.

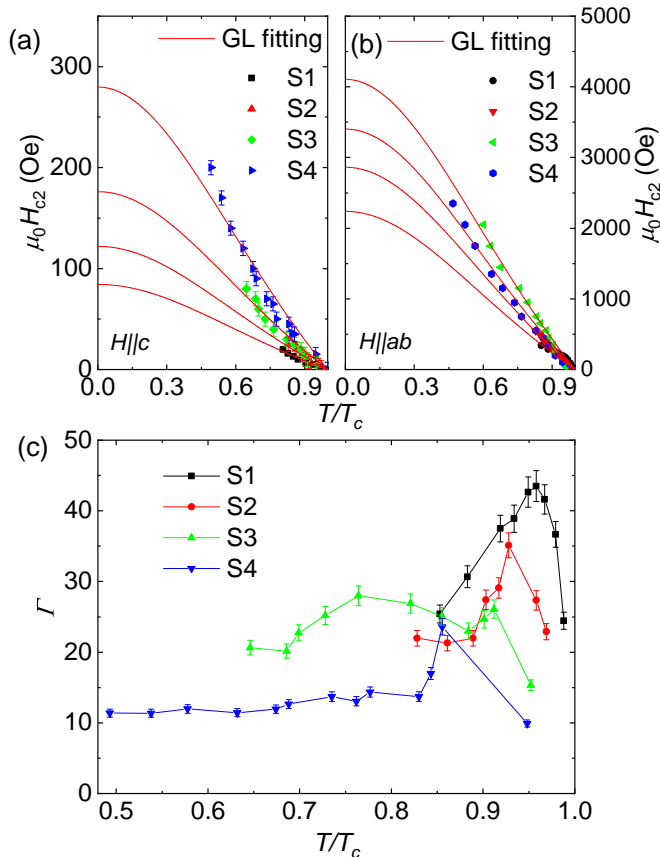


FIG. 4. Out-of-plane (a) and in-plane (b) upper critical fields with the GL fitting (solid line). (c) The anisotropy ratio $\Gamma = H_{c2}^{\parallel ab}/H_{c2}^{\parallel c}$ for four samples, all larger than 12.

C. Anisotropic superconductivity

In Fig. 3, superconductivity of samples is observed at low temperature. The superconducting transition temperature ($T_c^{50\%}$) is 0.34 K, 0.36 K, 0.48 K, and 0.69 K for samples S1, S2, S3, and S4, respectively, which is extracted by 50% drop of normal-state resistivity. T_c in In_xTaS_2 is a little smaller than $T_c \sim 0.8$ K in 2H-TaS₂ with the 3×3 CCDW at 78 K³⁶, and also smaller than $T_c = 0.91$ K for $\text{In}_{0.58}\text{TaSe}_2$ with two CDW transitions ($2 \times \sqrt{3}$ CCDW at 117 K and 2×2 CCDW at 77 K)². The lower T_c for In_xTaS_2 may be due to its higher 2×2 CCDW transition (130 K), which is higher than $\text{In}_{0.58}\text{TaSe}_2$. This is consistent with the typical phase diagram of CDW superconductors, i.e., Cu_xTiSe_2 ²⁶, in which T_c is enhanced upon suppressing CDW. The widths of superconducting transitions for samples S1 and S2 are much narrower than samples S3 and S4, indicating higher sample quality. The temperature dependence of resistivity under different magnetic fields are shown in Fig. 3 (b-i) for both H applied in the ab plane and along the c -axis.

TABLE I. Summary of physical parameters for the four In_xTaS_2 samples.

Sample	S1	S2	S3	S4
x	0.51	0.59	0.56	0.58
c (Å)	7.9647	7.9753	7.9773	7.9849
RRR	11.5	10.8	6.9	5.7
T_{CDW} (K)	132	130	131	126
$T_c^{50\%}$ (K)	0.34	0.36	0.48	0.69
$H_{c2}^{\parallel c}(0\text{K})$ (Oe)	84	122	176	280
$H_{c2}^{\parallel ab}(0\text{K})$ (Oe)	2238	2862	4106	3403
Γ (0K)	26	23	23	12
m_c/m_{ab}	676	529	529	144
ξ_c (nm)	7.4	7.0	5.9	8.9
ξ_{ab} (nm)	197.9	164.3	136.7	108.5
n (2K) ($\times 10^{27} \text{ m}^{-3}$)	1.82	4.66	2.61	5.63
ρ_0 ($\mu\Omega\text{cm}$)	25.1	9.3	13.6	9.1
k_F ($\times 10^9 \text{ m}^{-1}$)	3.3	4.5	3.7	4.8
l (nm)	29.8	42.7	43.2	38.7

The upper critical fields H_{c2} as a function of $T_c^{50\%}$ are summarized in Fig. 4(a) and (b), and approximately fitted by the Ginzberg-Landau (GL) model (solid lines), $H_{c2}(t) = H_{c2}(0)(1 - t^2)/(1 + t^2)$, where $t = T/T_c$. Taking the sample S1 for example, $H_{c2}^{\parallel ab}(0) = 2238$ Oe and $H_{c2}^{\parallel c}(0) = 84$ Oe, while the parameters of other samples are listed in Table I. Further effective mass can also be obtained according to the Lawrence-Doniach model^{37,38}, and the anisotropy ratio Γ is given by the following relation

$$\Gamma = H_{c2}^{\parallel ab}/H_{c2}^{\parallel c} = (m_c/m_{ab})^{1/2} = \xi_{ab}/\xi_c, \quad (1)$$

where m_c and m_{ab} are the effective mass tensor along the c axis and ab plane, respectively, and ξ_{ab} and ξ_c are the coherence length along the ab plane and c axis, respectively. The anisotropy ratio Γ vs. t of these samples are displayed in Fig. 4(c). The resultant Γ for samples are all larger than 12, implying the highly anisotropic superconductivity. The Γ value estimated at the extrapolated zero temperature is $\sim 26, 23, 23$, and 12 for samples S1, S2, S3, and S4 with different RRR , respectively, much larger than the most layered compounds, such as 2H-TaS₂³⁶ ($\Gamma = 6.7$ in Table II), typical iron-based superconductors (IBSs) [“122”-type $(\text{Ba,K})\text{Fe}_2\text{As}_2$ ($\Gamma < 2$)³⁹, “11”-type $\text{Fe}_{1+y}\text{Te}_{0.6}\text{Se}_{0.4}$ ($\Gamma < 1.8$), “1111”-type $\text{NdFeAsO}_{0.82}\text{F}_{0.18}$ ($\Gamma < 5$), “1144”-type $\text{RbEuFe}_4\text{As}_4$ ($\Gamma < 1.7$)⁴⁰, “112”-type $\text{Ca}_{1-x}\text{La}_x\text{FeAs}_2$ ($\Gamma < 4.2$)⁴¹], etc. Several TMDs-related compounds are listed in Table II. Unfortunately, the guided relation between T_c and layer distance d or Γ in these TMDs-related compounds seem not to be widely concluded. However, intercalated layered compounds seems a good method to possess highly anisotropic superconductivity and large $H_{c2}^{\parallel ab}$ in bulk state, even exceeding the Pauli limit H_p ^{31,42–44}.

According to the anisotropic Ginzburg-Landau formulas, $H_{c2}^{\parallel c} = \Phi_0/2\pi\xi_{ab}^2$ and $H_{c2}^{\parallel ab} = \Phi_0/2\pi\xi_{ab}\xi_c$, where Φ_0 is the flux quantum, the GL coherence lengths ξ_{ab}

TABLE II. Comparison of physical properties and anisotropy ratio of several TMD-related superconductors. Some compounds have two CDW transitions, which are denoted as T_{CDW1} and T_{CDW2} , respectively.

Material	T_c (K)	T_{CDW1} (K) (T_{CDW2})	c (Å)	Γ
2H-TaSe ₂ ⁴⁵	0.14	90 (121)	12.71	2.6
PbTaSe ₂ ³⁰	3.8	–	9.35	~4
In _{0.58} TaSe ₂ ²	0.91	77 (117)	8.3231	4.6
In _{0.51} TaS ₂	0.34	132	7.9647	>12
2H-TaS ₂ ³⁶	0.8	78	12.097	6.7
Na _{0.1} TaS ₂ ³¹	4.3	–	12.082	6.4
Cu _x TaS ₂ ⁴⁶	4.03	55	12.11	5.1

and ξ_c at zero temperature are calculated for four samples. The coherence length ξ_c perpendicular to the TaS₂ layer is more than 7 times larger than the distance $d = c = 7.9647\text{Å}$ between TaS₂ layers (Table I), illustrating that the superconductivity of In_xTaS₂ remains three dimensional in nature. The carrier density and ρ_0 at 2 K are estimated from R_H and low-temperature resistivity, respectively. The Fermi vector k_F and the mean free path ℓ are approximately inferred from the relation $\ell = \hbar k_F / \rho_0 n e^2$ and $k_F = (2\pi^2 n)^{1/3}$, respectively. All the physical parameters for four samples are summarized in Table I.

Due to the limit on the lowest temperature which we can reach in our measurements, the intrinsic anisotropy ratio may be a little overestimated, but its value is still supposed to be very large (> 10). Subsequently, a remarkably large effective mass ratio m_c/m_{ab} ($\gg 100$) can be extracted from Eq. (1). Taking into consideration of small $\gamma = m^* k_F k_B^2 / 3\hbar^2 = 43.76 \text{ J/m}^3/\text{K}^2$ from the Landau Fermi-liquid theory⁴⁷, which is obtained from the specific heat at constant volume, the geometric mean of effective mass m^* is approximately $2.2 m_e$, suggesting the possible small effective mass m_{ab} in the ab plane. The decreased effective mass may result from the linear band crossings (Weyl rings), which locate in the ab plane near the Fermi level due to the In vacancy.

IV. CONCLUSIONS

We systematically investigate anisotropic upper critical field in a nodal-line semimetal In_xTaS₂. Similar to

In_{0.58}TaSe₂, CDW, nodal-line topological states, and superconductivity coexist in In_xTaS₂. A 2×2 CCDW transition is observed at approximately 130 K supported by STM and transport measurements, and then superconducting transitions of four samples emerge in the temperature range between 0.34 K and 0.69 K.

Among these physical phases in this system, one of the interesting points is the gigantic anisotropy of upper critical field, which is significantly larger than that of 2H-TaS₂. Several origins may account for this property in 3D materials. In IBSs, the anisotropy ratio Γ appears to be related to the inter-layer coupling strength and the distance d between the charge reservoir layers and the conducting layers⁴¹. In the FeSe system, the larger Γ may result from the larger d , which is likely correlated with the higher T_c ⁴⁸. From the Lawrence-Doniach model, the anisotropic effective mass has an influence on the Γ value. Considering the lower T_c in this In-intercalated TaS₂ system, the origin of large Γ may be different from the IBSs system. We propose that the large Γ in In_xTaS₂ may result from gigantic anisotropic effective mass, because linear band crossings (Weyl rings) locate in the ab plane and reduce the effective mass tensor in this plane. The vacancy of In shifts Weyl rings much close to the Fermi level, and the superconducting gap may emerge in the Weyl rings as well. Therefore, we suppose the In-induced Weyl rings in this 112 system may contribute to the enhanced anisotropic effective mass, then generating the large superconducting anisotropy. This scenario may also be applied to the topological materials with similar band structures, such as In_xTaSe₂, PbTaSe₂, etc.

In addition, the correlation between the large anisotropic superconductivity and band crossing in topological materials deserves further investigation. Whether the superconducting gap emerges in the Weyl rings and the possible topological superconductivity also need further study.

ACKNOWLEDGMENTS

We thank Yongkang Luo, Ningning Liu for insightful discussions. This work was supported by the National Key R&D Program of the China (Grant Nos. 2016YFA0300402, 2019YFA0308602), the National Science Foundation of China (Grant Nos. 11774305) and the Fundamental Research Funds for the Central Universities of China.

-
- [1] A. A. Burkov, M. D. Hook, and L. Balents, Topological nodal semimetals, Phys. Rev. B **84**, 235126 (2011).
[2] Y. Li, Y. Wu, C. Xu, N. Liu, J. Ma, B. Lv, G. Yao, Y. Liu, H. Bai, X. Yang, L. Qiao, M. Li, L. Li, H. Xing, Y. Huang, J. Ma, M. Shi, C. Cao, Y. Liu, C. Liu,

- J. Jia, and Z.-A. Xu, Anisotropic gapping of topological Weyl rings in the charge-density-wave superconductor In_xTaSe₂, arXiv:2004.03441.
[3] G. Bian, T.-R. Chang, R. Sankar, S.-Y. Xu, H. Zheng, T. Neupert, C.-K. Chiu, S.-M. Huang, G. Q. Chang,

- I. Belopolski, D. S. Sanchez, M. Neupane, N. Alidoust, C. Liua, B. K. Wang, C.-C. Lee, H.-T. Jeng, C. L. Zhang, Z. J. Yuan, S. Jia, A. Bansil, F. C. Chou, H. Lin, and M. Z. Hasan, Topological nodal-line fermions in spin-orbit metal PbTaSe_2 , *Nat. Commun.* **7**, 10556 (2016).
- [4] L. M. Schoop, M. N. Ali, C. Straßer, A. Topp, A. Varykhalov, D. Marchenko, V. Duppel, S. S. P. Parkin, B. V. Lotsch, and C. R. Ast, Dirac cone protected by non-symmorphic symmetry and three-dimensional Dirac line node in ZrSiS , *Nat. Commun.* **7**, 11696 (2016).
- [5] Y. Wu, L.-L. Wang, E. Mun, D. D. Johnson, D. X. Mou, L. N. Huang, Y. B. Lee, S. L. Bud, P. C. Canfield, and A. Kaminski, Dirac node arcs in PtSn_4 , *Nat. Phys.* **88**, 667 (2016).
- [6] J.-M. Carter, V. V. Shankar, M. A. Zeb, and H.-Y. Kee, Semimetal and topological insulator in perovskite iridates, *Phys. Rev. B* **85**, 115105 (2012).
- [7] Z. K. Liu, B. B. Zhou, Y. Zhang, Z. J. Wang, H. Z. Weng, D. Prabhakaran, S.-K. Mo, Z. X. Shen, Z. Fang, X. Dai, Z. Hussain, and Y. L. Chen, Discovery of a three-dimensional topological Dirac semimetal, Na_3Bi , *Science* **343**, 864 (2014).
- [8] M. Neupane, S.-Y. Xu, R. Sankar, N. Alidoust, G. Bian, C. Liu, I. Belopolski, T.-R. Chang, H.-T. Jeng, H. Lin, A. Bansil, F. C. Chou, and M. Z. Hasan, Observation of a three-dimensional topological Dirac semimetal phase in high-mobility Cd_3As_2 , *Nat. Commun.* **5**, 3786 (2014).
- [9] H. Weng, C. Fang, Z. Fang, B. A. Bernevig, and X. Dai, Weyl semimetal phase in noncentrosymmetric transition-metal monophosphides, *Phys. Rev. X* **5**, 011029 (2015).
- [10] B. Q. Lv, H. M. Weng, B. B. Fu, X. P. Wang, H. Miao, J. Ma, P. Richard, X. C. Huang, L. X. Zhao, G. F. Chen, Z. Fang, X. Dai, T. Qian, and H. Ding, Experimental discovery of Weyl semimetal TaAs , *Phys. Rev. X* **5**, 031013 (2015).
- [11] S.-Y. Xu, I. Belopolski, N. Alidoust, M. Neupane, G. Bian, C. Zhang, R. Sankar, G. Chang, Z. Yuan, C.-C. Lee, S.-M. Huang, H. Zheng, J. Ma, D. S. Sanchez, B. Wang, A. Bansil, F. Chou, P. P. Shibayev, H. Lin, S. Jia, and M. Z. Hasan, Discovery of a Weyl fermion semimetal and topological Fermi arcs, *Science* **349**, 613 (2015).
- [12] D.-F. Xu, Y.-P. Du, Z. Wang, Y.-P. Li, X.-H. Niu, Q. Yao, P. Dudin, Z.-A. Xu, X.-G. Wan, and D.-L. Feng, Observation of Fermi arcs in non-centrosymmetric Weyl semimetal candidate NbP , *Chin. Phys. Lett.* **32**, 107101 (2015).
- [13] Z. Wang, Y. Zheng, Z. Shen, Y. Lu, H. Fang, F. Sheng, Y. Zhou, X. Yang, Y. Li, C. Feng, and Z.-A. Xu, Helicity-protected ultrahigh mobility Weyl fermions in NbP , *Phys. Rev. B* **93**, 121112(R) (2016).
- [14] Y. Li, Z. Wang, P. Li, X. Yang, Z. Shen, F. Sheng, X. Li, Y. Lu, Y. Zheng, and Z.-A. Xu, Negative magnetoresistance in Weyl semimetals NbAs and NbP : Intrinsic chiral anomaly and extrinsic effects, *Front. Phys.* **12**, 127205 (2017).
- [15] C. Fang, H. Weng, X. Dai, and Z. Fang, Topological nodal line semimetals, *Chin. Phys. B* **25**, 117106 (2016).
- [16] G. Bian, T.-R. Chang, H. Zheng, S. Velury, S.-Y. Xu, T. Neupert, C.-K. Chiu, S.-M. Huang, D. S. Sanchez, I. Belopolski, N. Alidoust, P.-J. Chen, G. Q. Chang, A. Bansil, H.-T. Jeng, H. Lin, and M. Z. Hasan, Drumhead surface states and topological nodal-line fermions in TiTaSe_2 , *Phys. Rev. B* **93**, 121113(R) (2016).
- [17] Y.-H. Chan, C.-K. Chiu, M. Y. Chou, and A. P. Schnyder, Ca_3P_2 and other topological semimetals with line nodes and drumhead surface states, *Phys. Rev. B* **93**, 205132 (2016).
- [18] C. Li, C. M. Wang, B. Wan, X. Wan, H.-Z. Lu, and X. C. Xie, Rules for Phase Shifts of Quantum Oscillations in Topological Nodal-Line Semimetals, *Phys. Rev. Lett.* **120**, 146602 (2018).
- [19] R. A. Molina and J. González, Surface and 3D quantum Hall effects from engineering of exceptional points in nodal-line semimetals, *Phys. Rev. Lett.* **120**, 146601 (2018).
- [20] S.-Y. Guan, P.-J. Chen, M.-W. Chu, R. Sankar, F. Chou, H.-T. Jeng, C.-S. Chang, and T.-M. Chuang, Superconducting topological surface states in the noncentrosymmetric bulk superconductor PbTaSe_2 , *Sci. Adv.* **2**, e1600894 (2016).
- [21] Y. Li and Z.-A. Xu, Exploring topological superconductivity in topological materials, *Adv. Quantum Technol.* **2**, 1800112 (2019).
- [22] J. L. Zhang, S. J. Zhang, H. M. Weng, W. Zhang, L. X. Yang, Q. Q. Liu, S. M. Feng, X. C. Wang, R. C. Yu, L. Z. Cao, L. Wang, W. G. Yang, H. Z. Liu, W. Y. Zhao, S. C. Zhang, X. Dai, Z. Fang, and C. Q. Jin, Pressure-induced superconductivity in topological parent compound Bi_2Te_3 , *Proc. Natl. Acad. Sci. U.S.A.* **108**, 24 (2011).
- [23] D. Kang, Y. Zhou, W. Yi, C. Yang, J. Guo, Y. Shi, S. Zhang, Z. Wang, C. Zhang, S. Jiang, A. Li, K. Yang, Q. Wu, G. Zhang, L. L. Sun, and Z. X. Zhao, Superconductivity emerging from a suppressed large magnetoresistant state in tungsten ditelluride, *Nat. Commun.* **6**, 7804 (2015).
- [24] Y. Li, C. An, C. Hua, X. Chen, Y. Zhou, Y. Zhou, R. Zhang, C. Park, Z. Wang, Y. Lu, Y. Zheng, Z. Yang, and Z.-A. Xu, Pressure-induced superconductivity in topological semimetal NbAs_2 , *npj Quantum Materials* **3**, 58 (2018).
- [25] Y. S. Hor, A. J. Williams, J. G. Checkelsky, P. Roushan, J. Seo, Q. Xu, H. W. Zandbergen, A. Yazdani, N. P. Ong, and R. J. Cava, Superconductivity in $\text{Cu}_x\text{Bi}_2\text{Se}_3$ and its implications for pairing in the undoped topological insulator, *Phys. Rev. Lett.* **104**, 057001 (2010).
- [26] E. Morosan, H. W. Zandbergen, B. S. Dennis, J. W. G. Bos, Y. Onose, T. Klimczuk, A. P. Ramirez, N. P. Ong, and R. J. Cava, Superconductivity in Cu_xTiSe_2 , *Nat. Phys.* **2**, 544 (2006).
- [27] M. S. Dresselhaus and G. Dresselhaus, Intercalation compounds of graphite, *Adv. Phys.* **51**, 1 (2002).
- [28] Y. P. Du, X. Y. Bo, D. Wang, E.-J. Kan, C.-G. Duan, S. Y. Savrasov, and X. G. Wan, Emergence of topological nodal lines and type-II Weyl nodes in the strong spin-orbit coupling system InNbX_2 ($X=\text{S,Se}$), *Phys. Rev. B* **96**, 235152 (2017).
- [29] S. S. Zhang, J.-X. Yin, G. Dai, L. Zhao, T.-R. Chang, N. Shumiya, K. Jiang, H. Zheng, G. Bian, D. Multer, M. Litskevich, G. Chang, I. Belopolski, T. A. Cochran, X. Wu, D. Wu, J. Luo, G. Chen, H. Lin, F.-C. Chou, X. Wang, C. Jin, R. Sankar, Z. Wang, and M. Z. Hasan, Field-free platform for Majorana-like zero mode in superconductors with a topological surface state, *Phys. Rev. B* **101**, 100507(R) (2020).
- [30] C.-L. Zhang, Z. J. Yuan, G. Bian, S.-Y. Xu, X. Zhang, M. Z. Hasan, and S. Jia, Superconducting properties

- in single crystals of the topological nodal semimetal PbTaSe₂, Phys. Rev. B **93**, 054520 (2016).
- [31] L. Fang, Y. Wang, P. Y. Zou, L. Tang, Z. Xu, H. Chen, C. Dong, L. Shan, and H. H. Wen, Fabrication and superconductivity of Na_xTaS₂ crystals, Phys. Rev. B **72**, 014534 (2005).
- [32] Y. Li, C. Xu, M. Shen, J. Wang, X. Yang, X. Yang, Z. Zhu, C. Cao, and Z.-A. Xu, Quantum transport in a compensated semimetal W₂As₃ with nontrivial Z₂ indices, Phys. Rev. B **98**, 115145 (2018).
- [33] D. Cho, S. Cheon, K.-S. Kim, S.-H. Lee, Y.-H. Cho, S.-W. Cheong, and H. W. Yeom, Nanoscale manipulation of the Mott insulating state coupled to charge order in 1T-TaS₂, Nat. Commun. **7**, 10453 (2016).
- [34] K. Bu, W. Zhang, Y. Fei, Z. Wu, Y. Zheng, J. Gao, X. Luo, Y.-P. Sun, and Y. Yin, Possible strain induced Mott gap collapse in 1T-TaS₂, Commun. Phys. **2**, 146 (2019).
- [35] Z. Dai, Q. Xue, Y. Gong, C. G. Slough, and R. V. Coleman, Scanning-probe-microscopy studies of superlattice structures and density-wave structures in 2H-NbSe₂, 2H-TaSe₂, and 2H-TaS₂ induced by Fe doping, Phys. Rev. B **48**, 14543 (1993).
- [36] R. C. Morris and R. V. Coleman, Anisotropic superconductivity in layer compounds, Phys. Rev. B **7**, 991 (1973).
- [37] W. E. Lawrence and S. Doniach, Proceedings of the 12th International Conference on Low Temperature Physics, Kyoto, 1970, edited by E. Kanda (Keigaku, Tokyo, 1971), p. 361.
- [38] Y. Jia, P. Cheng, L. Fang, H. Luo, H. Yang, C. Ren, L. Shan, C. Gu, and H.-H. Wen, Critical fields and anisotropy of NdFeAsO_{0.82}F_{0.18} single crystals, Appl. Phys. Lett. **93**, 032503 (2008).
- [39] H. Q. Yuan, J. Singleton, F. F. Balakirev, S. A. Baily, G. F. Chen, J. L. Luo, and N. L. Wang, Nearly isotropic superconductivity in (Ba,K)Fe₂As₂, Nature **457**, 565 (2009).
- [40] M. P. Smylie, K. Willa, J. K. Bao, K. Ryan, Z. Islam, H. Claus, Y. Simsek, Z. Diao, A. Rydh, A. E. Koshelev, W. K. Kwok, D. Y. Chung, M. G. Kanatzidis, and U. Welp, Anisotropic superconductivity and magnetism in single-crystal RbEuFe₄As₄, Phys. Rev. B **98**, 104503 (2018).
- [41] W. Zhou, J. C. Zhuang, F. F. Yuan, X. Li, X. Z. Xing, Y. Sun, and Z. X. Shi, Anisotropic superconductivity of Ca_{1-x}La_xFeAs₂ ($x \sim 0.18$) single crystal, Appl. Phys. Express **7**, 063102 (2014).
- [42] H. Bai, M. Wang, X. Yang, Y. Li, J. Ma, X. Sun, Q. Tao, L. Li, and Z.-A. Xu, Superconductivity in tantalum self-intercalated 4Ha-Ta_{1.03}Se₂, J. Phys.: Condens. Matter **30**, 095703 (2018).
- [43] H. Bai, X. Yang, Y. Liu, M. Zhang, M. Wang, Y. Li, J. Ma, Q. Tao, Y. Xie, G.-H. Cao, and Z.-A. Xu, Superconductivity in a misfit layered compound (SnSe)_{1.16}(NbSe₂), J. Phys.: Condens. Matter **30**, 355701 (2018).
- [44] H. Bai, L. Qiao, M. Li, J. Ma, X. Yang, Y. Li, Q. Tao, and Z.-A. Xu, Multi-band Superconductivity in a misfit layered compound (SnSe)_{1.16}(NbSe₂)₂, Mater. Res. Express **7**, 016002 (2020).
- [45] K.-I. Yokota, G. Kurata, T. Matsui, and H. Fukuyama, Superconductivity in the quasi-two-dimensional conductor 2H-TaSe₂, Physica B **284-288**, 551 (2000).
- [46] X. Zhu, Y. Sun, S. Zhang, J. Wang, L. Zou, L. E. DeLong, X. Zhu, X. Luo, B. Wang, G. Li, Z. Yang, and W. Song, Anisotropic intermediate coupling superconductivity in Cu_{0.03}TaS₂, J. Phys.: Condens. Matter **21**, 145701 (2009).
- [47] G. Baym and C. Pethick, *Landau Fermi-liquid theory: concepts and applications* (John Wiley & Sons, 2008).
- [48] S. Sun, S. Wang, R. Yu, and H. Lei, Extreme anisotropy and anomalous transport properties of heavily electron doped Li_x(NH₃)_yFe₂Se₂ single crystals, Phys. Rev. B **96**, 064512 (2017).